Research Square

Preprints are preliminary reports that have not undergone peer review.
They should not be considered conclusive, used to inform clinical practice,
or referenced by the media as validated information.

Intercalation of Ag ions into ammonium vanadate toward high-performance and long-lifespan aqueous zinc-ion battery cathodes

Yu Zhao
Tongcheng Teachers College
Xiu Wang
Tongcheng Teachers College
Yunyun Wang
Tongcheng Teachers College
Hongwei Wang
wanghongwei@tctc.edu.cn

Tongcheng Teachers College

Research Article

Keywords: Aqueous zinc-ion batteries, Ammonium vanadate, Defect engineering, Oxygen vacancies, Cathode materials

Posted Date: July 3rd, 2026

DOI: https://doi.org/10.21203/rs.3.rs-10006350/v1

License: This work is licensed under a Creative Commons Attribution 4.0 International License.
Read Full License

Additional Declarations: No competing interests reported.

Abstract

Aqueous zinc-ion batteries represent promising energy-storage devices for large-scale applications, yet the practical deployment of vanadate cathodes is greatly restricted by inferior rate capability and poor cyclic durability. Herein, a facile one-pot liquid-phase strategy is developed to fabricate Ag-doped ammonium vanadate, where Ag lattice doping simultaneously tailors the electronic configuration, introduces abundant lattice defects and stabilizes the intrinsic layered framework. Comprehensive characterizations verify that Ag incorporation triggers plentiful oxygen vacancies and low-valence V^{4+} active sites; meanwhile, intercalated Ag species act as interlayer pillars to enlarge Zn^{2+} diffusion pathways and strengthen structural robustness. Benefiting from such synergistic merits, the ANVO cathode delivers a high reversible capacity of 509.66 mAh g^{-1} at 0.5 A g^{-1} and retains 246.89 mAh g^{-1} even under an ultrahigh current density of 20 A g^{-1}. Impressively, a superior capacity retention of 92.17% is maintained after 2000 consecutive cycles at 5 A g^{-1}. Kinetic analyses confirm that Zn-ion storage is dominated by highly reversible capacitive contributions, which substantially accelerate the migration kinetics of charge carriers and Zn^{2+}. This work establishes a facile and effective metal-doping coupled defect-engineering methodology, offering an instructive route toward high-performance and long-lived vanadium-based cathodes for advanced aqueous zinc-ion batteries.

1. Introduction

Rechargeable aqueous zinc-ion batteries (AZIBs) have become one of the most promising candidates for large-scale energy storage due to their low cost, high intrinsic safety, abundant raw material reserves and eco-friendly advantages[1–3]. Nevertheless, their commercialization is still severely restricted by the drawbacks of cathode materials, such as low specific capacity, sluggish Zn^{2+} diffusion kinetics and inferior long-cycle stability[4–6]. Among various cathode candidates, layered ammonium vanadate ($NH_4V_4O_{10}$, NVO) exhibits great application potential owing to its large interlayer spacing, multi-electron redox characteristics of vanadium and high theoretical capacity, which enables fast Zn^{2+} insertion/extraction[7–9].

However, pristine NVO still suffers from inherent limitations. Excessive interlayer NH_4^+ ions inevitably block Zn^{2+} migration, and the layered structure is prone to irreversible pulverization and collapse during repeated cycling[10, 11]. Meanwhile, the insufficient active sites also lead to rapid capacity decay, greatly restricting its long-service-life application.

To address these issues, a variety of modification strategies have been developed to optimize the electrochemical performance of NVO, including cation pre-intercalation, microstructure regulation, oxygen vacancy engineering, heterostructure composite and metal ion doping[12–16]. Alkali/alkaline metal cations such as Na^+, K^+, Mg^{2+}, Al^{3+} and Rb^+ can serve as interlayer pillars to stabilize the layered framework[17–20]. Constructing nanobelt or flower-like architectures can shorten ion diffusion paths and

relieve structural stress[21, 22]. The introduction of oxygen vacancies can regulate electronic configuration and enrich active sites, while carbon or heterocomposite modification can effectively improve electrical conductivity and structural tolerance[23–26]. Even so, most existing strategies still suffer from single optimization effect, limited cycling improvement and complicated synthesis procedures.

Ion doping and defect engineering have been recognized as effective routes to optimize the layered framework, modulate electronic conductivity and enrich electrochemical active sites[27–29]. Rational metal ion doping can act as interlayer pillars to stabilize crystal structure, expand ion diffusion channels and reduce Zn^{2+} migration energy barrier[30–32]. In particular, Ag doping can induce abundant intrinsic lattice defects in NVO, create more available Zn^{2+} storage sites, optimize electronic structure and mitigate structural degradation during long-term cycling[33, 34]. Nevertheless, the synergistic mechanism of Ag doping in regulating lattice defects, active sites and cycling stability remains unclear, and the structural evolution and kinetic modulation still require further systematic exploration.

Herein, Ag-doped $NH_4V_4O_{10}$ (Ag-NVO) is successfully synthesized via a facile hydrothermal method. Ag ions act as stable interlayer pillars to maintain structural integrity, and simultaneously introduce rich lattice defects to increase electrochemical active sites and accelerate Zn^{2+} diffusion and charge transfer kinetics. Moreover, Ag doping optimizes the electronic structure and strengthens the structural rigidity, thereby suppressing structural deterioration and capacity fading during prolonged cycling. Consequently, the obtained Ag-NVO cathode delivers high specific capacity, superior rate capability and ultra-long cycle lifespan. This work provides a facile and effective strategy via Ag doping and defect engineering for the development of high-stability and long-life vanadium-based cathode materials toward advanced aqueous zinc-ion batteries.

2. Experimental section

2.1 Reagents

All chemical reagents used in this work were of analytical grade. Ammonium metavanadate (NH_4VO_3, 99.9%), silver nitrate ($AgNO_3$, 99.0%), polyvinylidene fluoride (PVDF) and N-methylpyrrolidone (NMP, 99.5%) were purchased from Adamas Biotechnology Co., Ltd. Zinc trifluoromethanesulfonate ($Zn(CF_3SO_3)_2$, 98%) was supplied by Alfa Aesar, and Ketjen black conductive carbon was provided by Nouryon Group.

2.2 Material Synthesis

Pure ammonium vanadate (NVO) and Ag-modified NVO (ANVO) samples were synthesized via a facile hydrothermal route. Typically, 2 mmol NH_4VO_3 was dissolved in 50 mL deionized water and stirred continuously at 75°C for 20 min until a pale yellow solution was formed. Dilute hydrochloric acid was then dropwise added to adjust the pH value to approximately 2, followed by the introduction of 0.5 mmol $AgNO_3$ under continuous stirring. The homogeneous precursor solution was transferred into a Teflon-

lined stainless steel autoclave and maintained at 180°C for 24 h. After natural cooling to room temperature, the precipitates were collected and repeatedly rinsed with absolute ethanol and deionized water. Finally, the products were dried overnight at 80°C to obtain dark-green ANVO powders. The pristine NVO was prepared through an identical procedure without the addition of silver nitrate, while all other experimental parameters remained unchanged.

2.3 Material Characterization

X-ray diffraction (XRD) patterns were recorded on a Rigaku SmartLab diffractometer with Cu Kα radiation over a scanning range of 5–80 degree at a rate of 5° min^{-1}. The morphological features and microstructural information were characterized by Hitachi SU8010 field-emission scanning electron microscopy (FESEM) and Thermo Talos F200 high-resolution transmission electron microscopy (HRTEM), coupled with energy-dispersive X-ray spectroscopy (EDS) for elemental distribution analysis. X-ray photoelectron spectroscopy (XPS) measurements were performed on a Thermo K-Alpha spectrometer to investigate the surface chemical states. Fourier-transform infrared spectroscopy (FTIR) was conducted on a Bruker Tensor II spectrometer to identify functional groups and chemical bonding configurations. Raman spectra were acquired using a Renishaw confocal Raman spectrometer to analyze lattice vibration and defect evolution.

2.4 Electrochemical Measurements

The working electrode was fabricated by mixing active material, Ketjen black, and PVDF at a mass ratio of 7:2:1 with NMP as the dispersant. The homogeneous slurry was uniformly coated onto 400-mesh stainless steel substrates with a diameter of 12 mm and dried at 80°C for 8 h. CR2016 coin-type cells were assembled in ambient air, employing zinc foil as the anode, 3 M aqueous solution as the electrolyte, and glass fiber as the separator. The areal mass loading of the active material was approximately 1.0 mg cm^{-2}. Galvanostatic charge–discharge and galvanostatic intermittent titration technique (GITT) measurements were carried out on a LAND CT2001A battery testing system. Cyclic voltammetry (CV) and electrochemical impedance spectroscopy (EIS) were tested on a CHI660E electrochemical workstation at various scan rates.

3. Results and discussion

To explore the structural evolution induced by Ag^{+} modification, X-ray diffraction (XRD) measurements were performed on pristine NVO and Ag-doped NVO-Ag samples, as presented in Fig. 1a. All diffraction peaks can be well assigned to the monoclinic phase (JCPDS No. 26–0096, space group C2/m), revealing the high phase purity of the as-prepared samples[35, 36]. A comparative analysis of the XRD patterns shows that no obvious variations in diffraction features are observed after ion introduction. This demonstrates that the crystal framework remains intact upon modification, and the intrinsic layered structure of ammonium vanadate is well preserved.

As depicted in Fig. 2a, the FTIR spectra of pristine NVO and Ag-modified ANVO are compared. The characteristic bands at 3239 and 3410 cm^{-1} are assigned to the N–H stretching vibrations originating from interlayer NH_4^+, whereas the absorption peak at 1401 cm^{-1} corresponds to the bending vibration of N–H bonds. Remarkably weakened intensities of these N–H-related peaks are detected for ANVO after Ag modification, demonstrating the intercalation of into interlayer spacing and partial substitution of intrinsic ammonium ions. The vibrational bands located at 540, 790 and 996 cm^{-1} are separately attributed to the bending vibration, antisymmetric stretching of bridging O–V–O bonds and terminal V = O double-bond stretching. Slight shifts of these V–O-related characteristic peaks verify the strong interfacial interaction between incorporated Ag species and vanadium–oxygen framework[37, 38].

As revealed by Raman spectra in Fig. 2b, pristine NVO presents negligible vibrational signals across the tested wavenumber range, while ANVO delivers an intense and sharp characteristic peak near 520 cm^{-1} originating from V–O–V linkage vibration. The lattice polarization triggered by Ag doping efficiently modulates local electronic configuration of the host material. Such structural regulation retains the intrinsic layered skeleton of vanadate and meanwhile dramatically alters the microscale bonding environment of vanadate groups[39].

X-ray photoelectron spectroscopy (XPS) was employed to reveal the modulation of elemental composition, oxygen vacancy concentration and vanadium valence state after Ag incorporation, and the relevant results are summarized in Fig. 3. The survey spectrum (Fig. 3a) only displays characteristic peaks of V and O for pristine NVO, whereas extra Ag-related signals emerge for Ag-modified ANVO, verifying the successful incorporation of Ag species into the ammonium vanadate host. As illustrated in the high-resolution Ag 3d spectrum (Fig. 3b), ANVO exhibits a pair of characteristic doublets at 373.0 eV (Ag $3d_{3/2}$) and 366.9 eV (Ag $3d_{5/2}$), while no Ag signal can be detected for bare NVO, further confirming the effective doping of Ag^+. The deconvoluted O 1s spectra (Fig. 3c) are split into lattice oxygen and defective oxygen components, with main peaks centered at 529.9 eV for NVO and 531.2 eV for ANVO. The remarkably enhanced proportion of defective oxygen in ANVO demonstrates that Ag doping triggers local lattice distortion and abundant oxygen vacancy formation[40, 41]. Owing to spin–orbit coupling, the V 2p spectrum is split into V $2p_{1/2}$ and V $2p_{3/2}$ subpeaks, each of which can be further fitted into V^{5+} and V^{4+} contributions. An elevated fraction of V^{4+} is observed in ANVO, originating from interfacial electron transfer between introduced Ag and the V–O framework, where partial V^{5+} is reduced to low-valence V^{4+} upon electron acquisition. The abundant oxygen vacancies and V^{4+} sites synergistically accelerate electron transportation and facilitate Zn^{2+} (de)intercalation kinetics, consequently improving the electrochemical energy storage capability of the electrode[42, 43].

SEM combined with TEM characterizations are adopted to uncover the microstructural features and crystalline information of the as-prepared samples. SEM observations verify that Ag-doped ANVO retains the intrinsic nanoribbon architecture of bare NVO, and the two samples share nearly identical morphological configuration (Fig. S1). TEM characterizations in Fig. 4 further analyze the microstructural

and crystalline properties of ANVO. The low-magnification TEM image (Fig. 4a) confirms the intact nanoribbon morphology, in good agreement with SEM observations. Numerous lattice defects can be explicitly spotted in HRTEM images (Fig. 4b and c), which stem from Ag doping and generated oxygen vacancies. The resolved interplanar distance of 0.35 nm coincides with the (110) crystal plane derived from XRD patterns, verifying that the fundamental crystal framework of NVO is well maintained after Ag incorporation. In addition, HAADF-STEM and corresponding elemental mapping (Fig. 4d-h) manifest homogeneous distribution of V, O, N and Ag throughout the whole nanoribbon, convincingly proving the successful uniform doping of Ag into the host lattice.

Coi

n cells were assembled using 2 mol L^{-1} aqueous $Zn(CF_3SO_3)_2$ electrolyte to evaluate the electrochemical energy storage properties of the as-prepared electrode. As revealed by cyclic voltammetry (CV) results in Fig. S2, two couples of distinct redox signals emerge at ~ 1 V and ~ 0.6 V, which originate from the reversible valence conversion of V^{5+}/V^{4+} and V^{4+}/V^{3+}, respectively, matching well with previous reports on pre-intercalated layered vanadium oxides[44, 45]. The weak redox peak located near 1.35 V is attributed to the reversible (de)intercalation of residual interlayer NH_4^+ within the crystal lattice. Such characteristic electrochemical signatures verify the successful synthesis of ammonium vanadate and the realization of its intrinsic redox activity.

GCD profiles of pristine NVO and Ag-modified ANVO at stepwise current densities ranging from 0.5 to 20 A g^{-1} are displayed in Fig. 5a and 5b, while the corresponding rate performance statistics are summarized in Fig. 5c and 5d. ANVO delivers superior discharge specific capacity over bare NVO across the entire tested current window. At 0.5 A g^{-1}, NVO and ANVO achieve discharge capacities of 359.88 and 509.66 mAh g^{-1}, respectively. As the current density sequentially rises to 1, 2, 5, 10 and 20 A g^{-1}, the specific capacities of NVO decay progressively to 317.11, 277.68, 252.80, 168.46 and 135.52 mAh g^{-1}, whereas ANVO retains comparatively higher values of 437.90, 371.25, 346.24, 287.84 and 246.89 mAh g^{-1}, with enlarged performance disparity at high rates. From the perspective of curve configuration, ANVO exhibits smoother charge/discharge plateaus with narrowed polarization gap relative to NVO; distinct redox plateaus can still be well preserved for ANVO even under an ultrahigh current of 20 A g^{-1}, in sharp contrast to the severely distorted plateaus and aggravated polarization of pristine NVO. When the current reverts back to 0.5 A g^{-1} after rate cycling, ANVO recovers its original capacity rapidly in Fig. 5c, verifying outstanding structural reversibility upon repeated Zn^{2+} (de)intercalation. Such prominent rate improvement originates from Ag incorporation: metallic Ag dopant elevates the intrinsic electronic conductivity of the V–O framework, meanwhile the in-situ generated oxygen vacancies and enriched V^{4+} sites expand Zn^{2+} diffusion pathways and accelerate ionic migration kinetics, endowing ANVO with remarkable Zn-storage capability at high current densities.

EIS and long-term cycling tests were implemented to systematically investigate the interfacial reaction kinetics and structural durability of pristine NVO and Ag-doped ANVO electrodes (Fig. 5e-g). As reflected

from Nyquist plots in Fig. 5e, the two electrodes exhibit comparable ohmic resistance (R_s), whereas ANVO possesses a much smaller charge-transfer resistance (R_{ct}=6.45 Ω) in contrast to 13.56 Ω for bare NVO, demonstrating that Ag doping optimizes electronic conductivity and lowers the kinetic barrier for interfacial Zn^{2+} migration. Cycling measurements (Fig. 5f and g) further verify the superior cycling robustness of ANVO. After 100 cycles at 0.5 A g^{-1}, NVO suffers a severe capacity decay with only 63.48% capacity retention, while ANVO retains a high retention of 92.09%. Even under rigorous cycling at 5 A g^{-1} over 2000 consecutive cycles, ANVO still maintains 92.17% of its initial capacity. Such remarkable cyclic stability originates from Ag-induced oxygen vacancies and abundant low-valence V^{4+} sites, which rigidify the layered lattice, suppress the dissolution of vanadium species and prevent structural collapse upon repeated Zn^{2+} (de)intercalation[46].

To uncover the favorable Zn^{2+} storage kinetics of ANVO, CV measurements at varied sweep rates were performed (Fig. 6a). All CV profiles acquired from 0.1 to 0.8 mV s^{-1} preserve analogous peak contours without obvious distortion, manifesting robust structural stability of the electrode under varying scanning conditions. Linear fitting between log(ip) and log(*v*) yields b-values of 0.80, 0.93, 0.93 and 0.84 for four redox peaks (Fig. 6b). These b-values ranging from 0.5 to 1 confirm that Zn-ion storage originates from the synergy of diffusion-controlled and capacitive-controlled processes, and the high b-values close to unity reveal the predominance of capacitive charge storage[47, 48]. Figure 6c presents the split curve of capacitive and diffusive currents at a representative sweep rate, while Fig. 6d quantifies their respective contribution ratios. As the sweep rate increases from 0.1 to 0.8 mV s^{-1}, the capacitive contribution gradually rises from 68% to 84%, whereas the diffusive contribution declines from 32% to 16%. The continuously enhanced capacitive fraction with elevated sweep rate corroborates that Ag doping generates abundant oxygen vacancies and low-valence V^{4+} active sites to boost interfacial capacitive reactions, which fundamentally accounts for the outstanding rate capability of ANVO electrode.

4. Conclusion

In summary, ANVO cathode was successfully fabricated via a facile hydrothermal method for high-performance aqueous zinc-ion batteries. Systematic characterizations confirm that Ag^{+} intercalation not only acts as interlayer pillars to stabilize the layered crystal framework but also induces abundant oxygen vacancies and enriches low-valence V^{4+} active sites, which significantly enhance electronic conductivity and accelerate Zn^{2+} diffusion kinetics. Electrochemical tests demonstrate that ANVO exhibits a high reversible capacity, excellent rate performance, and ultra-long cycling stability. Kinetic analysis reveals that the Zn^{2+} storage mechanism is dominated by fast capacitive behavior, which accounts for the outstanding rate capability. This work demonstrates that Ag doping combined with defect engineering is an effective strategy to boost the electrochemical performance of vanadate cathodes, providing a valuable reference for developing long-lifespan and high-power cathode materials for advanced aqueous zinc-ion batteries.

Declarations

Declaration of competing interest

The authors declare that they have no known competing financial interests or personal relationships that could have appeared to influence the work reported in this paper.

Author Contribution

Yu Zhao: Conceptualization, methodology, investigation, writing – original draft and revised manuscript. Xiu Wang: Investigation, electrochemical tests and materials characterizations, data curation, funding acquisition. Yunyun Wang: Literature research, auxiliary experiments, data curation. Hongwei Wang: Supervision, funding acquisition, project administration, writing – review and editing. All authors have read and approved the final manuscript.

Acknowledgments

This work was supported by the Scientific Research Project of the Education Department of Anhui Province (Key Project, Grant No. 2025AHGXZK30469).

References

1. Pan H, Shao Y, Yan P, Cheng Y, Han KS, Nie Z, Wang C, Yang J, Li X, Bhattacharya P, Mueller KT, Liu J (2016) Reversible aqueous zinc/manganese oxide energy storage from conversion reactions. Nat Energy 1:16039
2. Song M, Tan H, Chao D, Fan HJ (2018) Recent advances in Zn-ion batteries. Adv Funct Mater 28:1802564
3. Fang G, Zhou J, Pan A, Liang S (2018) Recent advances in aqueous zinc-ion batteries. ACS Energy Lett 3:2480–2501
4. Blanc LE, Kundu D, Nazar LF (2020) Scientific challenges for the implementation of Zn-ion batteries. Joule 4:771–799
5. Zhang N, Chen X, Yu M, Niu Z, Cheng F, Chen J (2020) Materials chemistry for rechargeable zinc-ion batteries. Chem Soc Rev 49:4203–4219
6. Ming J, Guo J, Xia C, Wang W, Alshareef HN (2019) Zinc-ion batteries: materials, mechanisms, and applications. Mater Sci Eng R 135:58–84
7. Tamilselvan M, Sreekanth TVM, Yoo K, Kim J (2021) Wide interlayer spacing ammonium vanadate (NH4)0.37V2O5·0.15(H2O) cathode for rechargeable aqueous zinc-ion batteries. J Ind Eng Chem 93:176–185

8. Liu JH, Wang Y, Chen X (2026) Ammonium vanadate-based cathodes for practical aqueous zinc-ion batteries: mechanisms, optimization, and challenges. Adv Funct Mater 36:e17823
9. Kundu D, Adams BD, Duffort V, Vajargah SH, Nazar LF (2016) A high-capacity and long-life aqueous rechargeable zinc battery using a metal oxide intercalation cathode. Nat Energy 1:16119
10. Li S, Yu D, Liu J (2023) Quantitative regulation of interlayer space of NH4V4O10 for fast and durable Zn2 + and NH4 + storage. Adv Sci 10:2206836
11. Gao X (2025) Break the trilemma: design of high-loading, high-capacity, high-stability zinc-ion battery cathode towards industrialization. PhD Thesis, University College London
12. Hao Z, Wang J, Feng J (2025) Insight into pre-intercalation of layered vanadium oxide cathodes: from precise control of the interspace to related electrochemical performance and beyond. Carbon Energy 7:e681
13. Zhang M, Wu H, Chang P (2025) Hybrid ternary co-intercalation in the interlayer of a vanadium oxide cathode enables high-capacity and stable zinc ion batteries. J Mater Chem A 13:15702–15712
14. Xia C, Guo J, Li P, Zhang X, Alshareef HN (2018) Highly stable aqueous zinc-ion storage using a layered calcium vanadium oxide bronze cathode. Angew Chem Int Ed 57:3943–3948
15. Wei T, Li Q, Yang G, Wang C (2018) An electrochemically induced bilayered structure facilitates long-life zinc storage of vanadium dioxide. J Mater Chem A 6:8006–8012
16. Yang Y, Fang Z, Wu S (2025) Achieving multiple structural optimizations of NH4V4O10 via Ca2 + intercalation for excellent zinc storage performance. J Alloys Compd 1035:181490
17. Soundharrajan V, Sambandam B, Kim S, Alfaruqi MH, Putro DY, Jo J, Kim S, Mathew V, Sun Y, Kim J (2018) Na2V6O16·3H2O barnesite nanorod: an open door to display a stable and high energy for aqueous rechargeable Zn-ion batteries as cathodes. Nano Lett 18:2402–2410
18. Tang B, Fang G, Zhou J, Wang L, Lei Y, Wang C, Lin T, Tang Y, Liang S (2018) Potassium vanadates with stable structure and fast ion diffusion channel as cathode for rechargeable aqueous zinc-ion batteries. Nano Energy 51:579–587
19. Ming F, Liang H, Lei Y, Kandambeth S, Eddaoudi M, Alshareef HN (2018) Layered MgxV2O5·nH2O as cathode material for high-performance aqueous zinc ion batteries. ACS Energy Lett 3:2602–2609
20. Zhang N, Dong Y, Jia M, Bian X, Wang Y, Qiu M, Xu J, Liu Y, Jiao L, Cheng F (2018) Rechargeable aqueous Zn-V2O5 battery with high energy density and long cycle life. ACS Energy Lett 3:1366–1372
21. Zong Q, Du W, Liu C, Du J, Yang M, Cao G (2021) Enhanced reversible zinc ion intercalation in deficient ammonium vanadate for high-performance aqueous zinc-ion battery. Nano-Micro Lett 13:116
22. Song J, Zhang Q, Yang G (2025) Biomimetic design for zinc-based energy storage devices: principles, challenges and opportunities. Chem Soc Rev 54:8071–8135
23. Liu C, Neale Z, Zheng J, Jia X, Huang J, Yan M, Tian M, Wang M, Yang J, Cao G (2019) Expanded hydrated vanadate for high-performance aqueous zinc-ion batteries. Energy Environ Sci 12:2273–2285

24. Li Y, Huang Z, Kalambate PK, Zhong Y, Huang Z, Xie M, Shen Y, Huang Y (2019) V2O5 nanopaper as a cathode material with high capacity and long cycle life for rechargeable aqueous zinc-ion battery. Nano Energy 60:752–759
25. Zhang Z, Wang Y, Guo T (2025) The influence of defect engineering on the electronic structure of active centers on the catalyst surface. Catalysts 15:651
26. Yang J, Li J, Li Y (2023) Defect regulation in bimetallic oxide cathodes for significantly improving the performance of flexible aqueous Zn-ion batteries. Chem Eng J 468:143600
27. Liu F, Fan Z (2023) Defect engineering of two-dimensional materials for advanced energy conversion and storage. Chem Soc Rev 52:1723–1772
28. Zhou J, Shan L, Wu Z, Guo X, Fang G, Liang S (2018) Investigation of V2O5 as a low-cost rechargeable aqueous zinc ion battery cathode. Chem Commun 54:4457–4460
29. Zhang Y, Tao L, Xie C (2020) Defect engineering on electrode materials for rechargeable batteries. Adv Mater 32:1905923
30. Yang Y, Tang Y, Liang S, Wu Z, Fang G, Cao X, Wang C, Lin T, Pan A, Zhou J (2019) Transition metal ion-preintercalated V2O5 as high-performance aqueous zinc-ion battery cathode with broad temperature adaptability. Nano Energy 61:617–625
31. Yoo G, Koo BR, An HR, Huang C, An GH (2021) Enhanced and stabilized charge transport boosting by Fe-doping effect of V2O5 nanorod for rechargeable Zn-ion battery. J Ind Eng Chem 99:344–351
32. Wang Y, Feng H, Zhang C (2025) Interlayer nanoarchitecture modification of layered materials in rechargeable metal-ion batteries. Electrochem Energy Rev 8:19
33. Fang Z, Tong Y, Yang Y (2024) Dual effects of Ag+ intercalation boosting the kinetics and stability of NH4V4O10 cathodes for enhanced zinc ion storage. Inorg Chem Front 11:8855–8865
34. Tang H, Wan K, Zhang K (2024) Boosting the zinc-ion storage capability of NH4V3O8 via cation-defect engineering. ACS Sustainable Chem Eng 12:13848–13860
35. Wang Z, Wang K, Nie K (2026) Three-dimensional through-localized amorphization engineering of crystalline/amorphous heterophase ammonium vanadate nanobelts for advanced aqueous zinc-ion batteries. Adv Funct Mater 36:e15102
36. Liu N, Li B, He Z, Dai L, Wang H, Wang L (2021) Recent advances and perspectives on vanadium- and manganese-based cathode materials for aqueous zinc ion batteries. J Energy Chem 59:134–159
37. Kakarla AK, Shankar EG, Bandi H (2026) Sodium ion intercalation in metal-organic-framework-derived porous V2O5 nanobelts toward durable and high-capacity cathode material for aqueous zinc-ion batteries. Small 22:e13892
38. Wang Y, Chen X, Liu JH (2026) Dual-functional nanoengineering via molecular pillaring and conductive hybridization for high-performance aqueous zinc-ion batteries. Chem Sci
39. Ponis J, Hariyani S, Agbeworvi G (2025) Single crystals of vanadium oxides as a lens for understanding structural and electronic phase transformations, ion transport, chemo-mechanical coupling, and electrothermal neuronal emulation. Chem Rev 125:10657–10764

40. Patil DR, Chavan HS, Lee A (2025) Enhancing the electrochemical catalytic performance of novel bifunctional oxygen vacancy-enriched silver niobate (AgNbO3) through electrochemical activation. J Mater Chem A 13:5945–5953
41. Yuan Y, Liu Y, Xie X (2023) 2D defect-engineered Ag-doped γ-Fe2O3/BiVO4: the effect of noble metal doping and oxygen vacancies on exciton-triggering photocatalysis production of singlet oxygen. Chemosphere 322:138176
42. Qian W, Chen Z, Zhu Y, Yang H, Sun Q, Zhou H, Zhou Z, Zhou Z, Huang J (2025) Oxygen-deficient vanadium oxides as the cathode for high-performance aqueous zinc-ion batteries. Chem Phys Lett 877:142271
43. Liu Y, Zhang Y, Jiang H (2022) Synergistic engineering of oxygen-defect and heterojunction boosts Zn2+ (de)intercalation kinetics in vanadium oxide for high-performance zinc-ion batteries. Chem Eng J 435:134949
44. Ghosh S, Jose N, Senthilkumar B (2021) Multi-redox (V5+/V4+/V3+/V2+) driven asymmetric sodium (de)intercalation reactions in NASICON-Na3VIn(PO4)3 cathode. J Electrochem Soc 168:050534
45. Liu JY, Cheng FY, Cui CY (2025) Decoupling pillar effect and electrostatic repulsion in layered NH4V4O10 for high efficiency zinc-ion storage. Sci China Chem
46. Zhu K, Yang W (2024) Vanadium-based cathodes for aqueous zinc-ion batteries: mechanisms, challenges, and strategies. Acc Chem Res 57:2887–2900
47. Wazir D, Naskar S, Sharmesh PR (2025) BiVO4/V2O5 heterostructures for durable and highly reversible calcium- and zinc-ion batteries. Sustain Energ Fuels 9:3954–3970
48. Yuan X, Zhang D, Lu H (2025) Synergistic enhancement effect of Maxwell polarization and preferential exposure of Zn(101) plane toward superhydrophobic separator for Ah-level zinc metal pouch batteries. Adv Sci 12:e06035

Figures

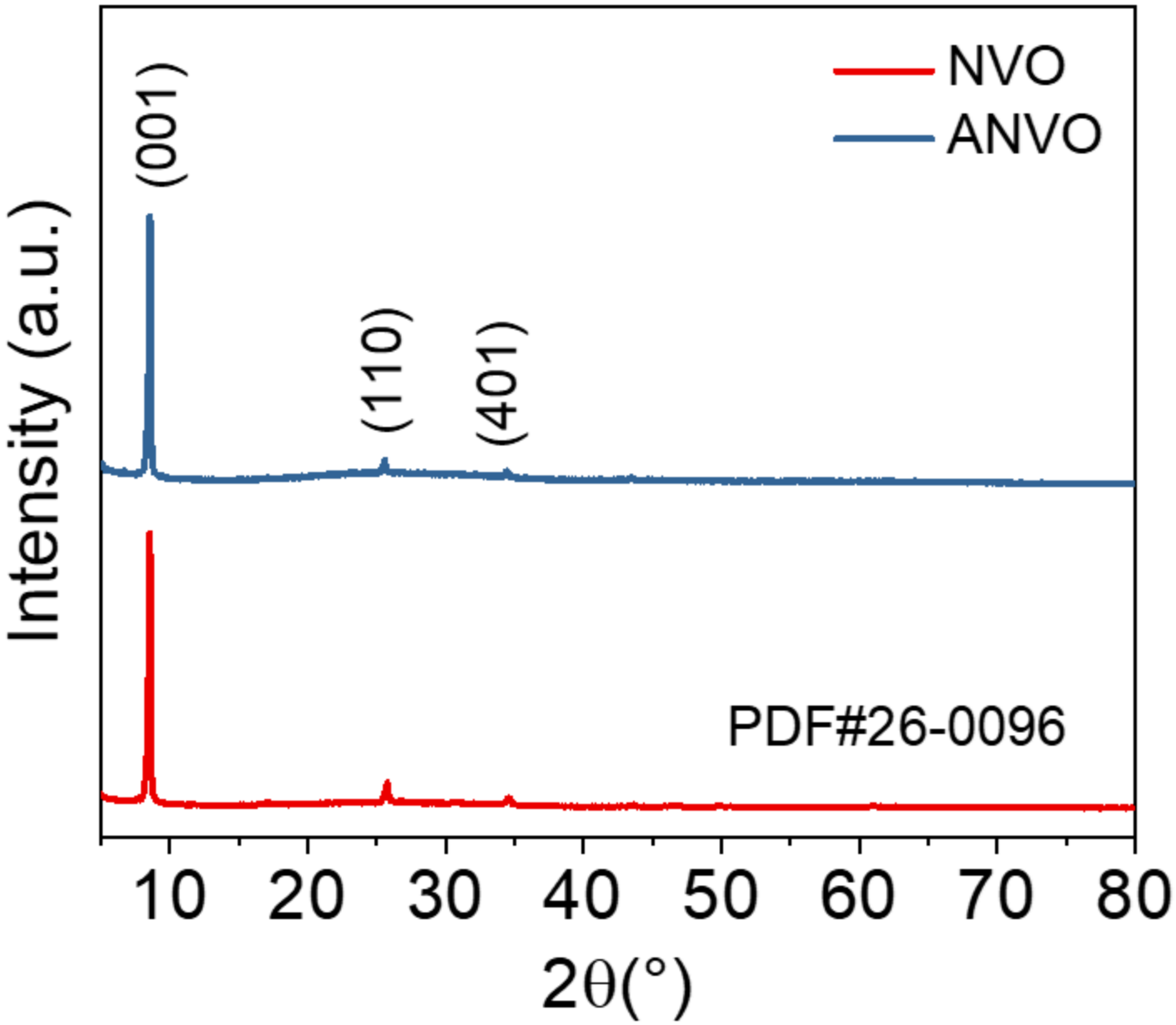


Figure 1

XRD patterns of pristine NVO and ANVO samples.

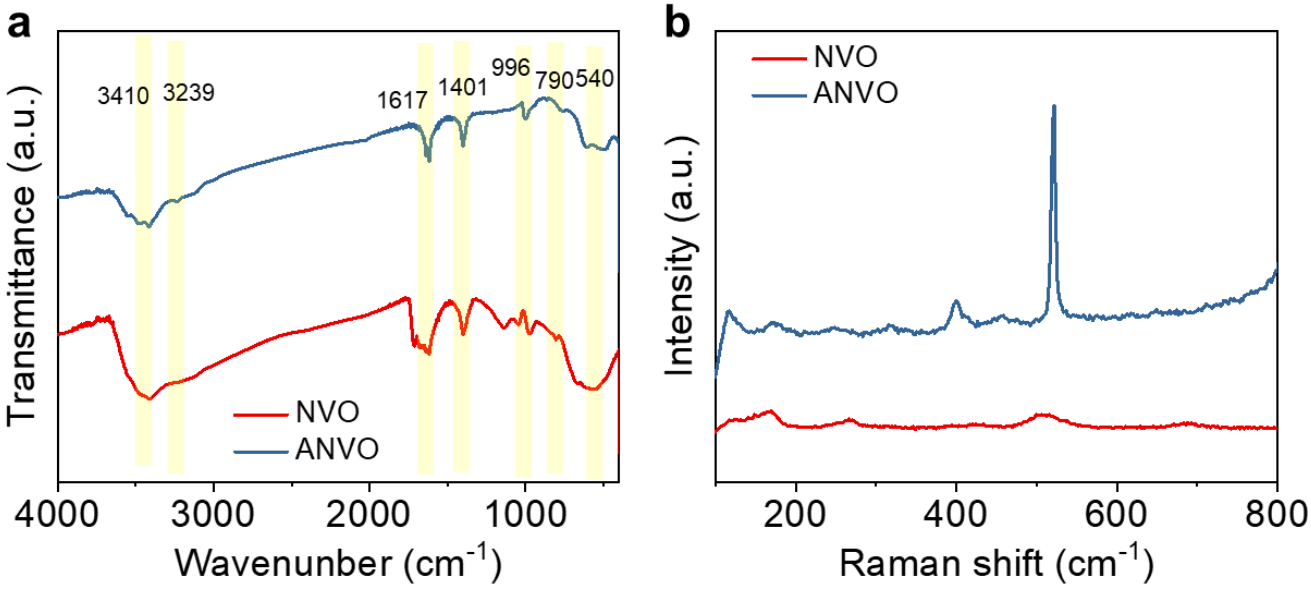


Figure 2

FTIR and Raman spectra of pristine NVO and Ag-modified ANVO samples.

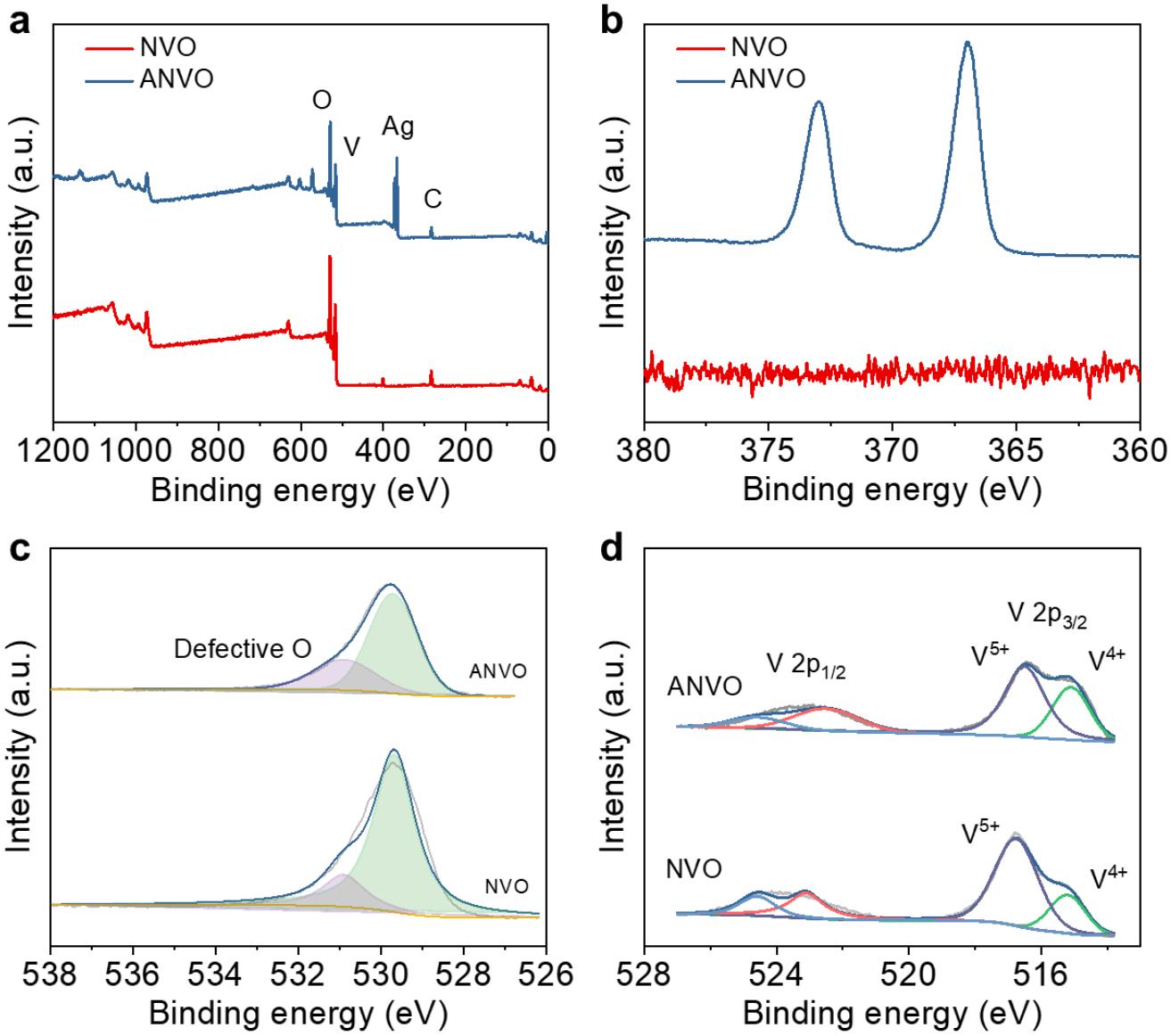


Figure 3

XPS spectra of pristine NVO and Ag-doped ANVO samples: (a) full survey spectrum, (b) Ag 3d, (c) O 1s and (d) V 2p high-resolution spectra.

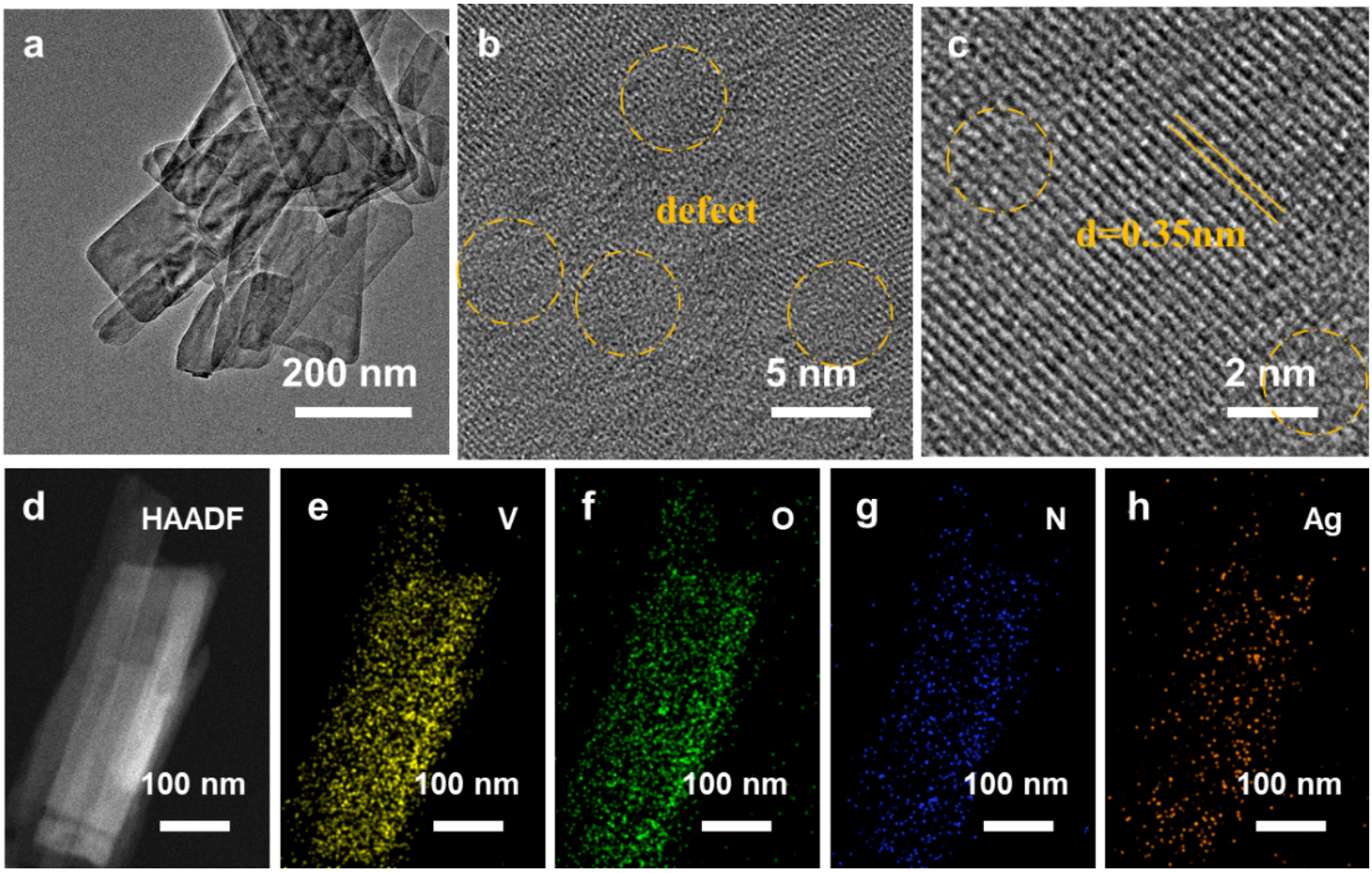


Figure 4

TEM and EDS-Mapping characterizations of ANVO: (a) low-magnification TEM image, (b,c) HRTEM images with lattice fringes and crystal defects, (d) HAADF-STEM image, and (e–h) corresponding elemental mapping of V, O, N and Ag.

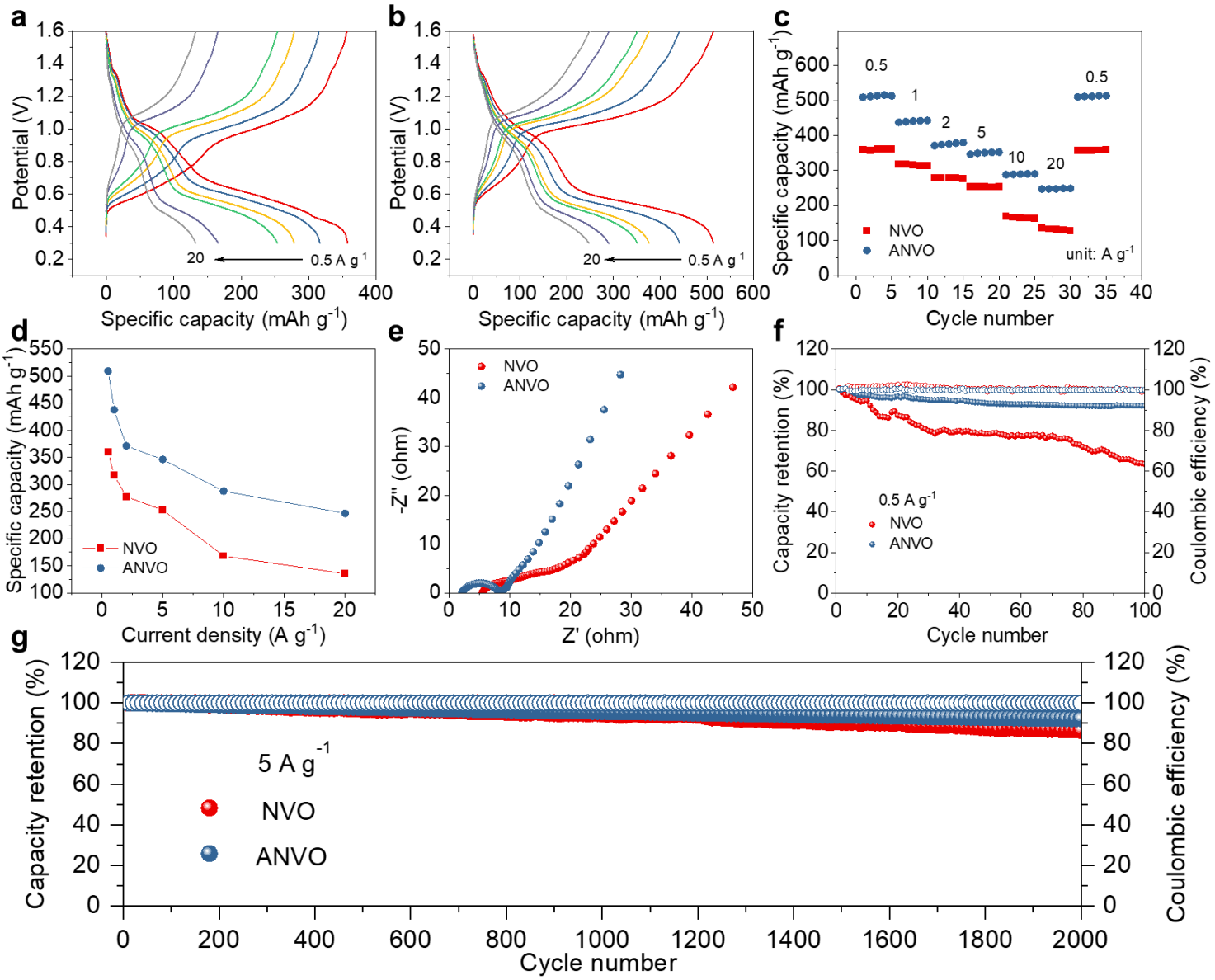


Figure 5

Electrochemical characterizations of NVO and ANVO electrodes: (a,b) Galvanostatic charge-discharge curves at varied rates, (c,d) rate capability, (e) EIS Nyquist plots, (f,g) cycling stability at 0.5 A g^{-1} and 5 A g^{-1}.

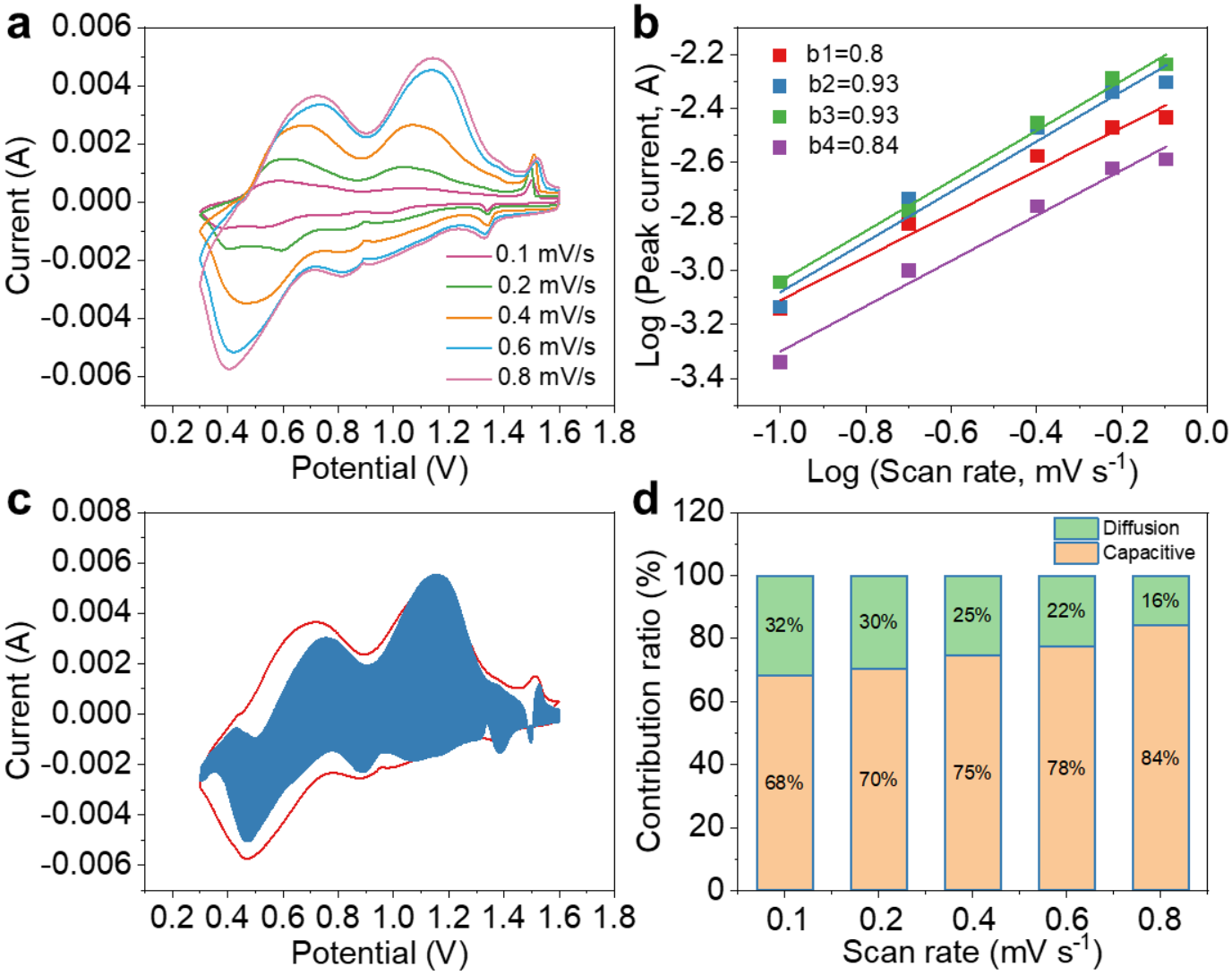


Figure 6

Kinetic characterization of ANVO: (a) CV profiles at various sweep rates, (b) log(i_p)-log(v) linear fitting for four redox peaks, (c) typical capacitive-diffusion separation curve, (d) quantitative contribution proportion at diverse scan rates.

Supplementary Files

This is a list of supplementary files associated with this preprint. Click to download.

- Supportinginformation.docx